Scaling and transition structure dependence on the fluid viscosity ratio in the selective withdrawal transition

Itai Cohen*

Department of Physics, University of Chicago, Chicago, Illinois 60637, USA
(Received 20 March 2003; revised manuscript received 3 May 2004; published 10 August 2004)

In the selective withdrawal experiment, fluid is withdrawn through a tube with its tip suspended above a two-fluid interface. At sufficiently high flow rates, the interface undergoes a transition so that the lower fluid is entrained with the upper one, forming a spout. Previous experiments address the scalings and similarity profiles characterizing steady states of the system near the transition for one combination of fluids. In the present study, we show that these scalings and similarity profiles extend to systems with different viscosity ratios. Surprisingly, we find no dependence of the scalings and similarity profiles on the lower fluid viscosity. We use the results of a low-Reynolds-number flow dimensional analysis to show that for different fluid combinations the curves denoting the transition straw height as a function of flow rate can be collapsed. Finally, these results are used to argue that in the low-Reynolds-number regime, the capillary length sets the scale for the final curvature of the interface before the transition.

I. INTRODUCTION

A look at Edgerton's photographic sequences [1] of the breakup of a drop interface as it drips from a faucet should instantly convince any skeptic that there is something fascinating about a fluid interface changing its topology, which hints at the richness of the underlying physics. Much attention has been devoted toward classifying these topological transitions in fluid systems [2–8] in the same manner as one classifies thermodynamic transitions. Cohen and Nagel [9] show that this established approach, used by others to study drop snap-off dynamics [10–12], extends to the study of steady-state interface profiles near the topological transition associated with selective withdrawal. In this paper, we describe how a change in the fluid viscosities affects the results of Cohen and Nagel.

In the selective withdrawal experiment a tube is immersed in a filled container so that its tip is suspended a height S above an interface separating two immiscible fluids (Fig. 1). When fluid is pumped out through the tube at low flow rates, Q, only the upper fluid is withdrawn. The flows deform the interface into an axisymmetric steady-state hump with a stagnation point at the hump tip (Fig. 1). The hump grows in height and curvature as Q increases (or S decreases) until the flows undergo a transition where the lower fluid becomes entrained in a thin axisymmetric spout along with the upper fluid. The interface becomes unbounded in the vertical direction, the stagnation point moves from the hump tip into the interior of the lower fluid, and the upper fluid geometry becomes toroidal thus changing the topology of the steady state. Once the spout has formed, an increase in Q (or decrease in S) causes the spout to thicken.

Near the transition, the steady-state mean radius of curvature at the hump tip, $1/\kappa$, can be orders of magnitude smaller

than the length scales characterizing the boundary conditions (for example the tube diameter, D). Fixing S and looking at the steady-state profiles as Q is increased, Cohen and Nagel observe that, up until the transition, both the hump curvature and height display scaling behavior characteristic of systems approaching a singularity. While similar scaling has been hypothesized for a system analogous to the 3D selective
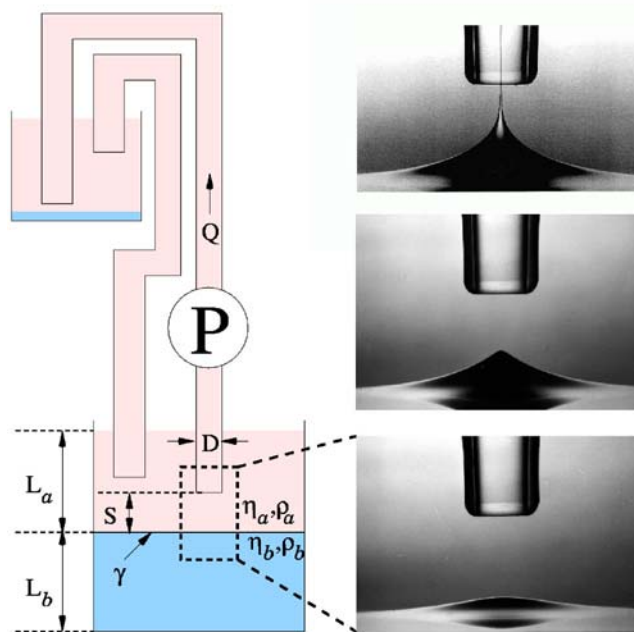

FIG. 1. Diagram of the experimental apparatus and photographs of the steady-state interface. Fluid is withdrawn from the withdrawal container and deposited into a waste container. The upper fluid is then siphoned back into the withdrawal container. Viewed bottom to top, the photographs show the evolution of the steady-state interface as Q is increased. The top photograph of the interface in the spout state is from Cohen *et al.* [13]. The middle photograph of the hump at the transition flow rate is from Cohen and Nagel [9].

————
*Present address: Harvard University, Cambridge, MA 02138, USA. Electronic address: icohen@deas.harvard.edu

70 026302-1

withdrawal system [14], this is the first time such scaling has been observed in the experiments. Cohen and Nagel then use the scaling relations to collapse the hump profiles near the transition onto a series of similarity curves. In doing so, they show that it is possible to treat the transition as "weakly-first-order." In Sec. IV, we show that the scalings and similarity profiles observed by Cohen and Nagel extend to systems with different viscosity ratios.

The manifestation of a true singularity would entail the divergence or vanishing of some physical quantities or length scales describing the system. However, for the range of parameters explored thus far, even when the system is arbitrarily close to the transition, κ remains finite. In Cohen and Nagel [9], a system near the transition with a surface tension of 31 dynes/cm and fluid viscosities of 1.7 and 2.9 P (1 P $\equiv 1$ g/(cm s)) for the upper and lower fluids, respectively, is shown to have a mean radius of curvature at the hump tip which is 200 μm.

Investigation of the viscosity-ratio dependence is clearly important for understanding the origin of the curvature cutoff in such systems. For the analogous 2D problem, which corresponds to replacing the tube with a line sink, Jeong and Moffatt [15] show that for an inviscid bottom fluid and viscous upper fluid, the 2D hump interface increases its curvature continuously with flow rate. Eggers [16] extends this theoretical result to show that when the lower fluid has a finite viscosity, this increase in curvature is cut off and the system undergoes a transition to a different steady state. In this new state, a sheet of the lower fluid is entrained along with the upper fluid into the line sink. However, the finite lower fluid viscosity prevents the 2D hump profiles from scaling onto a similarity solution. In contrast, Cohen and Nagel [9], in their 3D selective withdrawal experiments, do observe scaling behavior and profile collapse onto a similarity solution. Here, we show that performing the selective withdrawal experiments with a less viscous lower fluid does not get the system closer to the singularity. Furthermore, in Sec. V dimensional analysis is used to argue that the capillary length sets the scale for the value of the curvature cutoff, κ_u.

In the 2D system, the lower fluid viscosity dramatically affects the location of the transition to the Eggers solution [17]. In the selective withdrawal problem, nearly all of the experimental studies found in the literature are concerned with modeling large-scale extraction and use low-viscosity fluids to model the flows (see, for example, [18–23]). Therefore, the effects of viscous stresses in the experiments have remained unexplored. One exception arises in the modeling by Blake and Ivey [24] of magma layer mixing during volcanic eruptions. However, the fluids in these experiments are miscible. As pointed out by Lister [25], when surface tension is absent, there is always some fraction of the lower fluid that is extracted so that these experiments are not tracking the actual withdrawal transition. Cohen and Nagel's study takes into account the effects of the surface tension in an experiment mapping out the transition location for low Reynolds number flow. Here, that study is extended to address the dependence of the transition location on the fluid viscosities (Sec. V). For the range of parameters explored, only the upper fluid viscosity affects the transition location.

II. CHARACTERIZATION OF FLUIDS AND EXPERIMENTAL DETAILS

The parameters relevant for this experiment (see Fig. 1) are the upper and lower fluid viscosities and densities (η_a, η_b, ρ_a, ρ_b), the interfacial tension (γ), the orifice diameter (D), the height of the orifice above the interface (S), the flow rate (Q), the fluid height above the interface (L_a), the fluid layer depth below the interface (L_b), the container size, and the surfactant concentration.

The fluids used are heavy mineral oil (HMO), light mineral oil (LMO), silicone oil (polydimethylsiloxane, or PDMS, with an average molecular weight of about 31 000), salt water, and mixtures of glycerin and water. No surface chemistry is observed at the two-fluid interfaces even when the liquids remain in contact for periods longer than a month. However, a slight change in the transition flow rate at fixed S over a period of days indicates that the surfactant concentration at the interface increases with time. When the system is in the spout state, surfactants at the interface are "swept" into the straw. Leaving the system in the spout state for long periods of time, reduces the surfactant concentration over the entire interface. Once the surface has been cleaned, none of the results are significantly affected by the moderate increase in surfactant concentration, which occurs over a period of one week (see the Appendix for more details).

The viscosity η is measured using calibrated Cannon Ubbelohde viscometers immersed in a Cannon constant temperature bath. In this manner the viscosity can be determined to within ±5%. Glycerin can be diluted with water so that the resultant fluid has $0.01 \leqslant \eta \leqslant 14.9$ P [26]. The surface tension, γ, of the two-fluid interface is determined using the pendant drop method (see, for example, [27,28]), which takes advantage of the competition between the surface tension and buoyant forces acting on a static drop hanging from a nozzle. The buoyant forces distort the drop from a spherical shape. Measuring the distortion and density mismatch allows a determination of the surface tension. Implementation of this technique on water, toluene, and dimethylformamide shows a capability for measuring the surface tensions to within ±10%. The fluid systems studied and their properties are listed in Table I.

In the experiments, a large tank (30 cm × 30 cm × 30 cm) capable of holding fluid layers that are each about 12 cm in height is used as the withdrawal container. Fluid is pumped out of the withdrawal container and into a waste container. When the system is in the spout state, the fluids enter the waste container as an emulsion. This emulsion is deposited at the bottom of the waste container, which is where the droplets comprised of the lower fluid remain. The upper fluid is siphoned back into the withdrawal container at a rate that matches the withdrawal rate, thereby keeping L_a constant. The recycled fluid is deposited about 18 cm away from the region under investigation and does not affect the flows. L_b remains constant when the system is in the hump state and decreases with time when the system is in the spout state. However, even for thick spouts (0.1 mm in diameter) and for large flow rates (10 ml/sec) L_b decreases at the very slow rate of 0.01 mm/min which corresponds to a 0.1% change in the straw height, S.

TABLE I. List of the properties for each fluid system studied. Row 3 lists the symbols used in plotting the experimentally measured S_u curves in Figs. 3, 6, and 7. The last row lists the power-law exponent α used in fitting the curves in these figures.

	System 1	System 2	System 3	System 4	System 5	System 6	System 7
Upper Fluid	PDMS	PDMS	PDMS	PDMS	HMO	HMO	LMO
Lower Fluid	H_2O	Salt H_2O	Water/Glycerin	Glycerin	H_2O	Water/Glycerin	H_2O
S_u Symbol	●	+	⊡	◆	o	▼	▲
γ (dynes/cm)	43	40	29	23	35	31	34
ρ_a (g/ml)	0.97	0.97	0.97	0.97	0.87	0.87	0.85
ρ_b (g/ml)	1.00	1.11	1.24	1.26	1.00	1.24	1.00
Δ_ρ (g/ml)	0.03	0.14	0.27	0.29	0.13	0.37	0.15
η_a (g/cm s)	9.7	9.7	9.7	9.7	1.7	1.7	0.48
η_b (g/cm s)	0.010	0.013	2.9	12.3	0.010	2.9	0.010
η_b/η_a	1.0×10^{-3}	1.3×10^{-3}	3.0×10^{-1}	1.26	5.9×10^{-3}	1.7	2.1×10^{-2}
k_{usat}(1/cm)	12 ± 3	27 ± 7	22 ± 5	25 ± 5	31 ± 7	48 ± 10	5 ± 1
$k_{usat}l_c$	14 ± 5	14 ± 5	7 ± 3	7 ± 3	16 ± 5	14 ± 4	2 ± 1
α	0.44	0.42	0.41	0.40	0.32	0.30	0.30

The fluids are withdrawn using a rigid plastic pipet that is connected with tygon tubing to a B9000 Zenith metering gear pump with a variable speed DC motor. A Dynapar Rotopulser encoder is used to read out the withdrawal rate. The pump uses gears to displace fluid from the pump intake to the pump outlet. There are small variations in flow rate associated with the filling and draining of the gaps between the gear teeth. However, at large flow rates, or equivalently at high rotation frequencies, these variations damp out and the amplitude of the remaining noise corresponds to a very small percentage of the total flow rate. High rotation rates also average out the fluctuations in the driving motor. Using bigger or smaller pump attachments allows for pumping of the fluid at the same flow rate, but at a different gear rotation rate. This allows for the determination of the effects of noise in the flow rate on the transition. A further reduction of the noise in the experiments is achieved by siphoning the fluids into the waste container. However, when siphoning, the maximum rate of withdrawal is substantially smaller.

The apparatus is illuminated from the rear and a CCD video camera is used to image silhouettes of the steady-state hump shapes. The images are transferred onto a PC where an edge tracing IDL program tracks and records the points where the derivative of the pixel-intensity profile across the hump interface is extremized. The profiles are then superimposed onto the original images and checked for accuracy. In order to determine the mean curvature at the hump tip κ, either a Gaussian function or a parabola is used to fit the tip of the recorded hump profile. The value of κ is taken to be the curvature of the fitting function at the hump tip. However, depending on the width of the region chosen for the fit, the value of the measured curvature can vary by up to 50%. In order to make the choice of fitting region less arbitrary, first, the entire hump profile is fit with a Gaussian function. The fitting region is then taken to be one-tenth of the Gaussian decay length. Finally, the hump profile is fit with the parabola or Gaussian in the fitting region. Using this procedure the values of κ obtained from the Gaussian and parabolic fits are within 5% of each other. The curvatures reported in this paper are taken from the Gaussian fits.

Using this apparatus, we test the effects of the container walls and thickness of the upper fluid layer on the transition flow rate Q_u at constant S. Note that the switch in notation from S_u versus Q to Q_u versus S keeps the subscript with the variable that is being tuned when obtaining a given data point in the experiment. Figure 2(a) shows a plot of Q_u versus the distance L_w from one of the container walls while S is held constant. The fluid parameters for this particular experiment correspond to those of system 3 in Table I. For L_w greater than 2 cm there is very little variation in Q_u. Figure
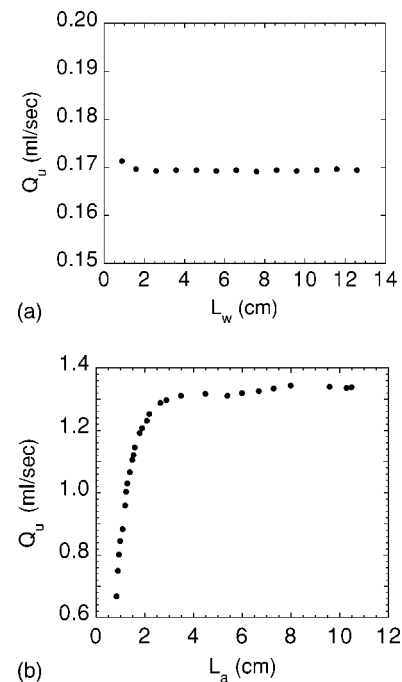

FIG. 2. (a) plots the transition flow rate Q_u versus the distance between the withdrawal tube and the container wall L_w for system 3 in Table I. (b) plots Q_u versus the upper fluid layer thickness L_a for system 5.

2(b) shows a plot of Q_u as a function of L_a for constant S. The fluid parameters correspond to those of system 5. As L_a is increased, Q_u first increases but eventually saturates and remains constant for L_a greater than about 3 cm. In all of the experiments L_b is typically kept at about 12 cm. Measurements of the transition flow rates show no significant variations between systems with an L_b of 12, 10, and 6 cm. Similar measurements for the Q_u dependence on L_w, L_a, and L_b are conducted for all of the different fluid combinations used in the experiments. For the tube diameters ($D=0.16$ cm and $D=0.79$ cm), tube heights (0.07 cm $< S < 2.0$ cm), and flow rates ($Q < 20$ ml/sec) used in the experiments, the container walls are kept sufficiently distant and the fluid layers are kept sufficiently thick so as not to affect the flows.

III. TRANSITION STRUCTURE AND HYSTERESIS

For the entire range of parameters explored thus far, the evolution of the steady-state hump profiles is cut off by the hump to spout transition before κ diverges. Cohen and Nagel show that for transitions occurring at low Q, or equivalently at small S_u, this cutoff is accompanied by a measurable hysteresis in the transition: the straw height at which the spout decays back into a hump is greater than S_u by a distance ΔS. As the system undergoes the transition at higher Qs, ΔS decreases exponentially and eventually becomes too small to measure. It is observed that the radius of curvature cutoff $1/\kappa_u$ has the same exponential decay with Q as does the hysteresis before saturating to a constant value $1/\kappa_{usat}$ at high Q. The curvature saturation values for all of the systems studied are shown in Table I.

When transitions occur at low S or Q, the ratio of the withdrawal tube diameter D to the straw height S is of order one. As a result, the straw diameter can set a length scale for $1/\kappa_u$. Figure 3 shows the effect of a factor of five increase in D on the S_u and $1/\kappa_u$ curves. The solid line in Fig. 3(a) is a fit to the $D=0.16$ data and has the form $S_u \propto Q^{0.3\pm0.05}$. The two S_u curves in Fig. 3(a) show no significant dependence on D. As shown by Cohen and Nagel [9], for the range of flow rates explored, ΔS is at least an order of magnitude smaller than S_u. Therefore, the variations due to the hysteresis are not expected to have a noticeable effect on the S_u values. The $1/\kappa_u$ curves in Fig. 3(b) are fit (dash dot) with the forms $1/\kappa_u=0.02+0.32\exp(-Q/0.032)$ and $1/\kappa_u=0.02+2.3\exp(-Q/0.22)$ for the $D=0.16$ cm and $D=0.79$ cm data sets, respectively. The onset of the flat asymptotic dependence for $1/\kappa_u$ occurs at higher Q for larger straw diameters. This evidence indicates that the initial decrease in $1/\kappa_u$ results from the finite width of the withdrawal tube. Consequently, there is more than one mechanism responsible for the transition cutoff. At large values of S_u these finite size effects vanish and the value of $1/\kappa_u$ is determined by the fluid parameters. The discussion of scaling behavior for the hump profiles is restricted to this regime.

IV. COMPARISON OF SCALING ANALYSIS AND SIMILARITY SOLUTIONS

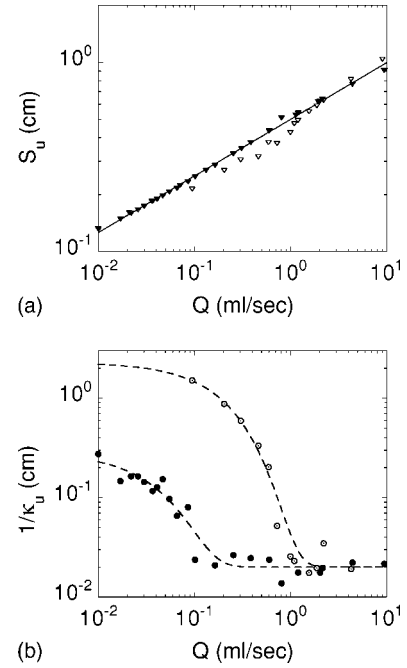In order to determine the effects of η_b on the transition structure, we compare the Cohen and Nagel scaling and

FIG. 3. Plots of S_u (a) and $1/\kappa_u$ (b) as a function of Q for two different tube diameters D. The open symbols depict the curves for system 6 with $D=0.79$ cm. For comparison, the closed symbols reproduce the Cohen and Nagel [9] data for system 6 with $D=0.16$ cm.

similarity solution results for system 6 to those of system 5 where η_b is 300 times smaller. The scaling analysis comparison in the next subsection focuses on how κ changes as the transition is approached. This analysis is, therefore, localized to the hump tip. The hump profiles can be collapsed onto similarity curves as described in Sec. IV B. The similarity curve comparison focuses on the shape of the profile beyond the hump tip. In Sec. IV C we describe the connection between the treatments.

A. Scaling analysis of hump curvature reveals the same exponents

For a given straw height, as Q is increased the hump profile grows in height h_{max} and curvature κ. Figure 4(a) plots h_{max} versus κ for four representative data sets taken at different S. The data suggests that for each curve, as h_{max} approaches its asymptote h_c, κ diverges. Indeed, it is observed that for all straw heights $(h_c-h_{max})/h_{max} \propto \kappa^\beta$. Here, the value of h_c is used as a fitting parameter. Note that the transition cuts off the evolution of the hump states preventing the system from getting arbitrarily close to the singularity and limiting the precision with which the exponents β can be determined. The power laws for curves corresponding to different S have different prefactors. We, therefore, divide κ by the power-law prefactor n in order to collapse the curves onto a single-scaling curve. The physical interpretation of the constants $n(S)$ is given in Sec. IV B. Figure 4(b) plots $(h_c-h_{max})/h_{max}$ as a function of the normalized curvature κ/n. The excellent collapse indicates that all of the divergences
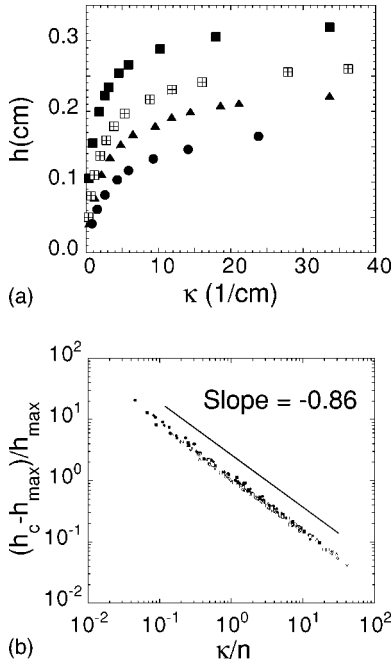
FIG. 4. Scaling for the hump mean curvature κ and height h_{max} for fluid system 5 in Table I. (a) plots h_{max} versus κ for data sets corresponding to four representative straw heights. (b) plots (h_c $-h_{max}$)/h_{max} versus κ/n for the entire data set corresponding to 20 different straw heights. The line corresponds to a power law with an exponent of −0.86.

have the form $(h_c-h_{max})/h_{max}=(\kappa/n)^\beta$ with $\beta=-0.86\pm0.10$. For system 6 Cohen and Nagel obtain $\beta=-0.85\pm0.09$.

B. Similarity solutions show hump profiles are identical

For any given S, the value of h_c taken from the scaling relations for the hump height and curvature can be used to collapse the hump profile shapes near the transition onto a similarity curve. Cohen and Nagel define the scaled variables as follows:

$$H(R) = \frac{h_c - h(r)}{h_c - h_{max}} \quad \text{and} \quad R = \frac{r\kappa}{n}. \quad (1)$$

Here $h(r)$ is the hump profile and r is the radial coordinate. This transformation shifts and scales the profiles so that the cusp of the singular solutions is positioned at the origin and the maximum hump heights are located at $H=1$ and $R=0$. Figure 5(a) overlays eight hump profiles for the S $=0.667$ cm data set. Figure 5(b) shows the same profiles after scaling. Excellent collapse of the hump profiles is observed. A power-law fit to the scaled profiles in the region beyond the parabolic hump tips [solid line in Fig. 5(b)] shows that $H(R)=(\kappa/n)^x$ with $x=0.72\pm0.10$. For system 6 Cohen and Nagel observe that $x=0.72\pm0.08$.

Figure 5(c) shows a comparison of the similarity solutions for five different tube heights. These profiles all display the same power-law dependence. Here, n [taken from Fig. 4(b)] is used to scale the radial components of these profiles and obtain good collapse for curves corresponding to different
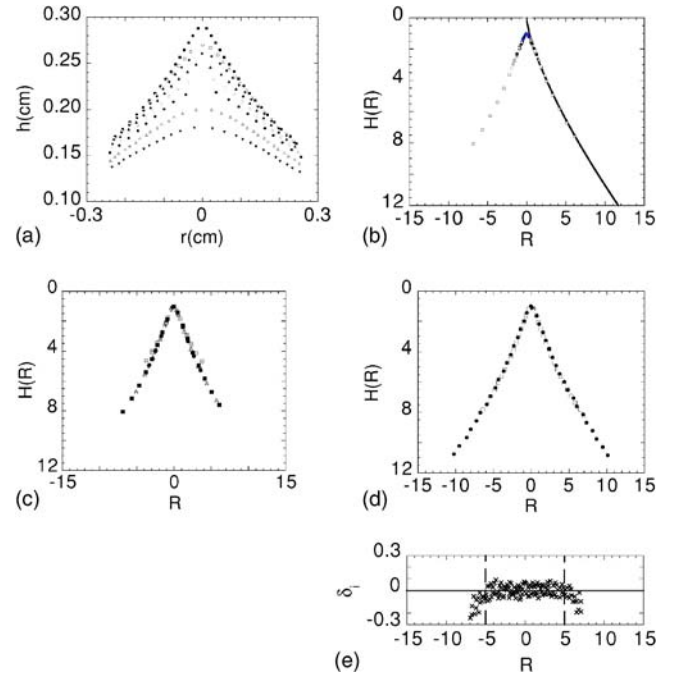

FIG. 5. The scaled hump profiles for system 5 along with a comparison of the similarity profiles for systems 5 and 6. (a) shows eight profiles taken from the $S=0.667$ data set for system 5. (b) shows the same profiles after scaling. The solid line corresponds to a power law of the form $R^{0.72}$. (c) compares the similarity curves for the $S=0.984$ cm, 0.921 cm, 0.889 cm, 0.667 cm, and 0.445 cm data sets. (d) overlays the similarity profiles for system 5 with S $=0.667$ (open symbols) and system 6 with $S=0.830$ (closed symbols). (e) shows a plot of the residual quantity δ_i for the data points in (d). The region between the vertical dotted lines corresponds to the similarity regime where the residuals become centered around zero.

straw heights. The constants n decrease with increasing S indicating that the profiles become shallower at large S. The decrease is roughly described by the relations $n\approx11$ $\exp(-2.5S)$ and $n\approx10$ $\exp(-2.5S)$ for systems 5 and 6, respectively. The origin of this dependence is not understood. The points of deviation for the $S=0.445$ cm profile (crossed box symbol), mark the transition from the similarity regime to the matching regime beyond which the profiles become asymptotically flat. At large enough radii all of the scaled profiles display these deviations.

As a final check, Fig. 5(d) shows a comparison of the the system 6 similarity profile for $S=0.831$ cm and the system 5 similarity profile for $S=0.667$ cm. Figure 5(e) plots the residuals δ_i, which correspond to the minimum distance between each point on the system 6 curve and the value of a local linear fit to the system 5 curve at the same R value. An error analysis calculation for the data points located between $-5<R<5$ (where δ_i are centered around zero) shows that $\chi^2\approx1.6$ [36]. This χ^2 value indicates that the differences between the two similarity curves are on the same order as the experimental uncertainty, which is taken to be a quarter of a scaled pixel. This error analysis, in conjunction with the close agreement between the power-law exponents x and the

prefactors n indicates that the similarity solutions describing the profiles of systems 5 and 6 are nearly identical.

C. The localized scaling relations predict the form of the similarity solutions

The scaling relation in Fig. 4(b) can be used to predict the exponent x in the power-law fits to the similarity solutions in Figs. 5(b)–5(d). Inserting the observed scaling dependence for the hump tip $(h_c - h_{max})/h_{max} = (\kappa/n)^\beta$ into the observed form of the similarity profile $H(R) = R^x$, the following relation is obtained:

$$\frac{h_c - h(r)}{h_{max}}\left(\frac{\kappa}{n}\right)^{-\beta} = r^x\left(\frac{\kappa}{n}\right)^x. \qquad (2)$$

Since, for a given r, the functions $[h_c - h(r)]/h_{max}$ and r^x have constant values, x must equal $-\beta$. More intuitively, for a given S, as Q is increased, the parabolic-tip regions decrease their radial length scale at a rate tracked by the term n/κ and are simultaneously pulled toward the singularity in the axial direction at a rate tracked by the term $(h_c - h_{max})/h_{max}$ leaving behind power-law profiles with exponents that reflect the scaling observed in Fig. 4(b).

Recall that the fits to the similarity profiles gave the exponents $x = 0.72 \pm 0.10$. and $x = 0.72 \pm 0.08$ for systems 5 and 6, respectively. Both of these exponents are within error (although slightly smaller) of the exponents observed in the scaling relations which gave the exponents $-\beta = 0.86 \pm 0.10$ and $-\beta = 0.85 \pm 0.09$ for systems 5 and 6, respectively. The slight differences between the values of the exponents $-\beta$ and x in both systems imply that the similarity profile may be influenced by the matching region, which connects the local similarity solutions with the flat interface at $r \to \infty$. Such effects are known to manifest themselves in the coating of thin threads [29]. There, threads pulled through a fluid medium are coated with a thin film whose thickness, under the right conditions, is determined by the matching of the local solution to the static nonlocal meniscus at $r \to \infty$.

What sets the value of the exponents β and x? Typically, the observed scaling dependencies in these types of problems result from the balance of the relevant stresses in the region where the curves collapse onto similarity solutions. For example, a scaling analysis where the viscous stresses of the upper and lower fluids balance the stress arising from the interfacial curvature predicts linear scaling dependencies and conical profile shapes [11]. The nonlinearity of the observed dependencies and the lack of dependence of the similarity solution on η_b indicate that a different stress balance may govern the flows (e.g., viscous stress due to upper fluid balances the stress due to the interface curvature).

The comparisons described in this section have shown that the only difference between the scaling dependencies and similarity solutions is a 10% increase in the value of the power law prefactors $n(S)$ for system 5. With the exception of this slight difference, the comparison demonstrates that for this range of viscosity ratios, η_b does not affect the scaling relations and similarity profiles near the selective withdrawal transition. Thus, the 3D problem is fundamentally different from the analogous 2D problem, where a small but
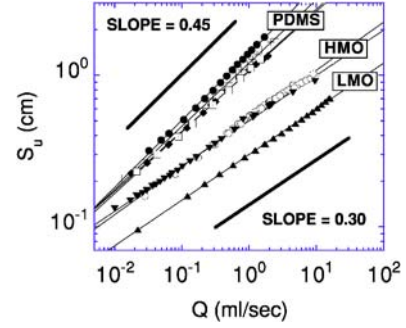

FIG. 6. Plots of the transition tube height S_u as a function of Q for the seven systems listed in Table I. For each system, it is observed that $S_u \propto Q^\alpha$ with α ranging between 0.30 and 0.45. The S_u curves cluster into three groups corresponding to the different upper fluids used in the experiments. Each cluster is labeled with the corresponding upper fluid.

finite lower fluid viscosity dramatically affects the nature of the singularity.

V. MAPPING OUT THE TRANSITION LOCATION

Having shown that the viscosity ratio does not affect the scaling relations and similarity profiles, we turn to the question of whether S_u is affected by such a change in the parameters. In this section we compare the transition location for seven fluid systems. The data from the experiments are presented in the next subsection. In Sec. V B, dimensional analysis is used to deduce which dimensionless combinations of the experiment parameters collapse the data for the transition curves. We then use the results of this dimensional analysis to try and address which parameters set the length scale for the cutoff curvatures κ_{usat} in Sec. V C. Finally, in Sec. V D we present a crude but suggestive comparison of these results with Lister's [25] simulations of selective withdrawal for zero-Reynolds-number flow.

A. Data show that the transition location is unaffected by η_b

Figure 6 shows a plot of S_u versus Q for seven pairs of fluids. There are a few obvious trends. The three distinct clusters of curves in Fig. 6 correspond to different values of η_a. For a given value of Q, a sixfold increase in η_a, increases S_u by about a factor of two. Second, for a given value of Q, even a 1000-fold increase in η_b does not significantly affect S_u. These observations indicate that for the range of parameters studied, it is η_a rather than the viscosity ratio that affects the transition location within the S versus Q parameter space. Finally, all of the data sets show that $S_u \propto Q^\alpha$ where α ranges between 0.30 and 0.45. The values of α are listed in Table I.

The remaining trends due to changes in $\Delta\rho$ and γ are weak. Furthermore, surfactants can shift the S_u curves by an amount comparable to the shifts seen in the curves forming the uppermost cluster in Fig. 6. Therefore, either simulations or more careful measurements of S_u will be necessary to resolve the roles of these parameters.
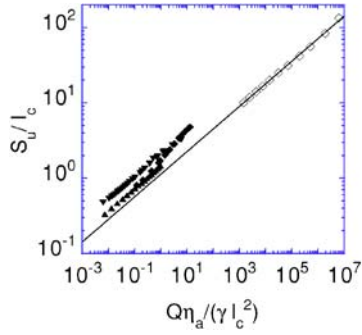
FIG. 7. Plot of the experimentally measured S_u/ℓ_c versus $(Q\eta_a)/(\gamma\ell_c^2)$ curves along with the curve predicted by the simulations of Lister [25]. The closed symbols depict the experimental measurements for systems 4, 6, and 7 in Table I, while the open symbols depict the range of $(Q\eta_a)/(\gamma\ell_c^2)$ over which the simulations are performed. The solid line represents a power-law fit to the simulation results and has a slope of 0.30.

B. Dimensional analysis leads to scaling of transition curves

In general, S_u is a function of the parameters: $Q, \eta_a, \eta_b, \rho_a, \rho_b, \Delta\rho g, \gamma, D$. However, in these experiments neither D nor η_b affect the value of S_u. Therefore, the dependence on these parameters, the viscosity ratio, and the various aspect ratios containing D can be eliminated. According to Buckingham's Pi theorem, the remaining seven variables must be functions of four dimensionless variables. Without a theory it is difficult to determine which dimensionless combination describes the flows. However, the fact that η_a plays a fundamental role in determining the transition location suggests that the flows may be in the low Reynolds number regime. Note that an assumption of low-Reynolds-number flow would eliminate the variables ρ_b and ρ_a and reduce the number of dimensionless variables to two.

To check the validity of such an assumption the Reynolds number characterizing the different systems must be determined. There are a variety of ways in which the Reynolds number for the flows in the hump state can be defined [37]. Here, the balance between the capillary stress, which acts to smooth the interface, and the viscous stress, which deforms the interface, is used to make the estimate [38].

At the hump tip the fluid velocity vanishes. The fluid velocity in the absence of the interface $Q/\{2\pi[S-h(0)]^2\}$, is used to estimate the fluid velocity away from the hump tip v_{bulk}. The length d over which the velocity decreases to zero can be estimated from the stress balance $\gamma\kappa = \eta_a v_{bulk}/d$. The dimensionless combination $\rho_a v_{bulk} d/\eta_a$ is then used to estimate the Reynolds number Re. For the data in Fig. 6, $Re \lesssim 1\times 10^{-4}$ for the top cluster of curves, $Re \lesssim 3\times 10^{-2}$ for the middle cluster of curves, and $Re \lesssim 4$ for the lowest curve.

Having validated the assumption of low-Reynolds-number flow for the majority of the data, we eliminate the variables ρ_b and ρ_a. Dimensional analysis of the remaining variables in this problem indicates that

$$S_u/\ell_c = f\left(\frac{Q\eta_a}{\gamma\ell_c^2}\right) \tag{3}$$

where f is a function to be determined and $\ell_c \equiv \sqrt{\gamma/\Delta\rho g}$. The solid symbols in Fig. 7 depict the S_u/ℓ_c versus $(Q\eta_a)/(\gamma\ell_c^2)$

curves for the systems with $\eta_a = 9.7$ P, $\eta_a = 1.7$ P, and $\eta_a = 0.48$ P corresponding to systems 4, 6, and 7 in Table I. For clarity, we only show one curve from each of the clusters in Fig. 6. The curves for all the other systems fall between the curves for systems 6 and 7. The data in Figs. 6 and 7 indicate that the function f has the form of a power law with an exponent α which varies between 0.30 and 0.45. It is noteworthy that under this scaling, the experiment data sets collapse onto each other to within a factor of two in $(Q\eta_a)/(\gamma\ell_c^2)$.

C. Dimensional analysis predicts that the capillary length determines κ_{usat}

In the 2D problem, η_b plays a fundamental role in determining the curvature cutoff [17]. Table I shows that the asymptotic value of κ_u for system 6 is 1.5 times larger than the value of κ_{usat} for system 5. This weak trend is opposite the one found in the 2D analog, and shows that changing η_b by over two orders of magnitude has virtually no effect on the value of κ_{usat}. Since κ_u is independent of the flow rate at large S, an increase in the capillary number $\eta_a Q/[\pi(D/2)^2\gamma\rho_a]$ can also be ruled out as a method of getting the system closer to the singularity.

The dimensional analysis presented in the previous section can help determine which parameters set the value of κ_{usat}. In the low-Reynolds-regime, κ_{usat} must have the form:

$$\frac{1}{\kappa_{usat}\ell_c} = p\left(\frac{Q\eta_a}{\gamma\ell_c^2}\right) \tag{4}$$

where p is a function to be determined. Using the observation that κ_{usat} is independent of the flow rate, this analysis predicts that $1/\kappa_{usat} \propto \ell_c$. This result is surprising since (with the exception of the system 7 data) ℓ_c is typically over an order of magnitude larger than $1/\kappa_{usat}$. Nevertheless, a comparison of $\kappa_{usat}\ell_c$ values for systems 1–6 (see Table I) indicates that the values are within about one standard deviation of the average $\kappa_{usat}\ell_c$ value for these six systems. System 7 shows a significantly smaller value of $\kappa_{usat}\ell_c$. A comparison of systems 7 and 5 shows that while ℓ_c is held constant, the value of κ_{usat} changes by a factor of six. Shallow hump profiles are also observed for nearly inviscid systems, which use air as the upper fluid and water as the lower fluid. For the flow rates at which κ_{usat} for system 7 asymptotes, $Re \approx 1$. Therefore, it is possible that the value of κ_{usat} for system 7 is measured at flow rates that are too large for the low-Reynolds-number assumption to be valid. A low-Reynolds-number simulation, which can vary ℓ_c by orders of magnitude, would allow for a more detailed study of the effect of ℓ_c on κ_{usat}. The dependence of κ_{usat} on ℓ_c also means that the final curvature should change as the local boundary conditions are varied [30].

D. Comparison with results of zero-Reynolds-number simulations

For completeness, we compare these experiment results with Lister's simulations of selective withdrawal for zero-Reynolds-number flow [25]. These are the only currently

available simulations where the viscous effects of the upper fluid are taken into account. However, many aspects of this comparison remain crude:

(i) The simulations are designed to model a system with a point sink that is located many capillary lengths, ℓ_c, away from the interface. While S_u shows no dependence on the tube diameter D, [see Fig. 3(a)], it is still comparable to the capillary length. Thus, the experiments are performed at much smaller values of Q and S_u than the simulations making it impossible to compare the results quantitatively. Nevertheless, since it is expected that S_u is a smooth function of Q, one can check that the simulation and experiment data sets are consistent with this expectation.

(ii) Lister's simulations are performed for equal viscosity fluids. However, the fact that in these experiments η_b does not affect the transition location can be used to compare the simulations with the experiments for which the fluid viscosities are unequal.

(iii) In the simulation, a point sink is used to withdraw the fluids. However, in the experiments, the tube can only withdraw fluid from below the tube orifice. Therefore, the simulation results will overestimate the flow rate at which the transition occurs.

Clearly, more detailed simulations which address these concerns would allow for a better comparison. With these caveats in mind, we proceed with the comparison to Lister's zero-Reynolds-number simulation results.

Figure 7 overlays the simulation results onto the rescaled transition data. The open symbols depict the range of $(Q\eta_a)/(\gamma\ell_c^2)$ over which the simulations are performed. The simulations are conducted using dimensionless variables so that the resulting prediction is independent of the particular fluid parameters describing the different experimental systems. The solid line represents a power-law fit to the simulation results. This fit is projected into the regime where the measurements are taken in the experiments. As expected, the fit to the simulation data overestimates the transition flow rate. Note that a factor of two reduction in the simulation flow rate is sufficient to shift the simulation prediction onto the experiment results. However, it is not clear if a simple reduction in the flow rate can fully account for the different withdrawal geometries. Nevertheless, it is suggestive that the curve predicted by the simulation has a value of $\alpha=0.30$, which agrees with the values of α for systems 5–7.

Finally, even though under scaling, the data for the $\eta_a=9.7$ P system rests in between the scaled curves for systems 6 and 7, a discrepancy remains between the power-law exponent describing this system (0.45) and the numerical prediction (0.30). It is unlikely that the effects of fluid inertia can account for this variation. First, the fluids with the lower viscosities follow the zero-Reynolds number prediction more closely. If inertial stresses were playing a role, one would expect the α values for the lower viscosity systems to deviate from the prediction. Second, since a large change in Re can also occur along the S_u versus Q curves, one would expect the effects of inertia to manifest as variations in the slope. Such variations are not observed.

An alternative scenario, is that the high-extensional strain rate causes up to a threefold increase in the upper fluid viscosity as Q is increased. Such an effect could result from a small population of high molecular weight PDMS chains [31] in the upper fluid bath [32]. Since increasing η_a causes an upward shift in the S_u versus Q curves, a viscosity that increases with Q would result in a higher power law exponent α. Unfortunately, current state-of-the-art techniques are not sensitive enough to measure such weak viscosity dependencies in these relatively low viscosity fluids. Therefore, to investigate such effects, it may be useful to measure how α changes when a high molecular weight polymer is introduced into the upper fluid bath.

VI. CONCLUSIONS

In this paper, it has been shown that the transition straw height for a given flow rate S_u changes as $S_u \propto Q^\alpha$, where α ranges between about 0.45 and 0.30. Experiments comparing S_u for different systems of immiscible fluids with flows reaching into the low-Reynolds-number regime have been performed. The data indicate that for viscosity ratios less than one, the upper fluid viscosity rather than the viscosity ratio determines the value of S_u. The scaling of the data suggested by dimensional analysis in the low-Reynolds-number regime shows that to within a factor of two in $(Q\eta_a)/(\gamma\ell_c^2)$, the transition data can be collapsed onto a universal curve (Fig. 7). This curve is slightly shifted from the curve predicted by the simulations of Lister for zero-Reynolds-number flows with a point sink. However, a factor of two reduction in the simulation flow rate seems to account for this shift. While this comparison is not conclusive, it is suggestive and indicates that a theory tailored to address the concerns outlined in Sec. V D may be able to more accurately account for the observed dependencies.

For low flow rates, where the withdrawal tube is sufficiently close to the interface, the transition is hysteretic. Cohen and Nagel have correlated the decrease in the hysteresis for transitions taking place at higher S with the decrease in the final mean radius of curvature $1/\kappa_u$. Here, it has been shown that the tube diameter, at low S, sets a length scale for $1/\kappa_u$. As S is increased, $1/\kappa_u$ decreases and eventually saturates to $1/\kappa_{usat}$ implying that the residual discontinuity in the transition depends on the fluid parameters rather than the experiment geometry. As Table I shows, the value of κ_{usat} does not depend on η_b for the range of viscosities investigated. It is in the asymptotic regime where $1/\kappa_u$ has reached its asymptote $1/\kappa_{usat}$ that the scaling behavior and similarity profiles are investigated.

We have performed a detailed comparison of the scaling relations for systems 5 and 6 that have the same upper fluid viscosity but have a lower fluid viscosity, which is different by a factor of 300. It is observed that up until the cutoff, the hump profiles behave as though they are approaching a singular solution where, at a critical flow rate, the hump height would be equal to h_c and the mean curvature κ would diverge. The quantity $(h_c - h_{max})/h_{max}$ has been shown to scale as $(\kappa/n)^\beta$ where $\beta=-0.85\pm0.09$ and $\beta=-0.86\pm0.10$ for the high and low η_b systems, respectively. These scaling relations are used to collapse the hump profiles for different flow rates and straw heights near the transition onto a series of similarity curves. The region of the similarity profiles located
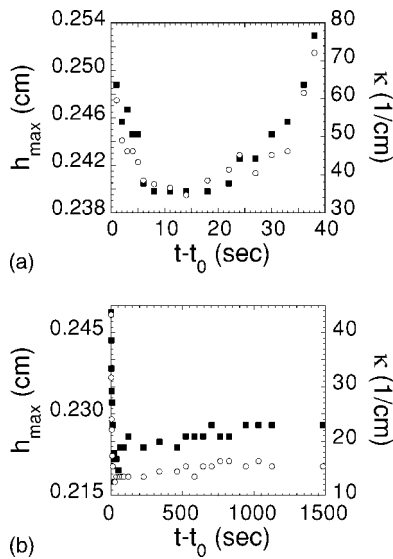
FIG. 8. Plots of the time dependence for h_{max} (squares) and κ (open circles) just after spout collapse for system 3. The figures correspond to measurements taken at constant S but at different Qs. In both figures, t_0 corresponds to the time at which the spout collapses into a hump. (a) shows measurements for a system close to the transition with $(Q_c - Q)/Q \approx 0.004$. (b) shows measurements for a system slightly farther away from the transition with $(Q_c - Q)/Q \approx 0.01$.

beyond the parabolic tip can be fit with a power law that has an exponent $x = 0.72 \pm 0.10$ and $x = 0.72 \pm 0.08$ for the curves in systems 5 and 6, respectively. The results show that for the range of viscosities investigated, both the scaling exponents and the shape of the similarity solution are independent of η_b and the viscosity ratio. In fact, a direct comparison of the similarity solution for both fluid systems indicates that, within error, the curves are identical. The lack of η_b dependence for the S_u versus Q curves κ_{usat} the similarity profiles n, and the scaling exponents x and β indicates that the selective withdrawal problem is very different from its 2D analog.

The similarity treatment for the hump profiles is localized to the hump tip, which is over an order of magnitude smaller than ℓ_c. This separation of length scales between the hump radius of curvature and the boundary conditions is a typical requirement for a successful similarity treatment. If κ_{usat} does indeed depend on ℓ_c, then the matching region, which connects the profile near the tip of the hump to the flat interface at large radii, may be responsible for setting the length scale for the cutoff. Such an effect could also explain the slight difference between the observed value of the power-law exponent describing the similarity solution (x) and the value predicted by the scaling relations (β). Control over the cutoff curvature is crucial for obtaining more accurate scalings. Moreover, this control could be used to adjust the minimum spout diameter and advance emerging technologies, such as coating microparticles [13], creating monodispersed microspheres [33], and emulsification through tip streaming [6,34], which take advantage of a selective withdrawal geometry. The importance of identifying which parameters determine the length scale for the cutoff warrants a more careful investigation of the k_{usat} dependence on ℓ_c and the local interfacial boundary conditions.

Finally, the robustness of the similarity solution shows that singularities can be used to organize the study and classification of the steady-state hump profiles near the selective withdrawal transition. In particular, the discontinuous nature of the transition, marked by the cutoff curvature κ_u, coupled with the display of scaling behavior suggests a transition structure that is remarkably similar to that of weakly first-order thermodynamic transitions. Whether this analogy hints at some deeper relationship between the classification schemes for weakly first-order thermodynamic transitions and the classification schemes for these types of topological transitions remains to be shown.

APPENDIX: SURFACTANT EFFECTS

Surfactants can significantly affect interfacial tension and surface flows. In the present studies there are two effects that result from the presence of surfactants. First, measurements taken after the surfactant concentration at the interface is allowed to equilibrate for a period of a week show a uniform 20% increase in S_u, or, equivalently, a 50% decrease in the transition flow rate. Upon cleaning the interface once again, the S_u data points return to their original value. The observed shift in S_u resulting from the differing surfactant concentration is quite small compared with the shift observed when η_a is increased by a factor of five. Nevertheless, the fact that the transition flow rate can change by nearly 50% depending on the surfactant concentration is noteworthy.

The second noticeable effect due to surfactants is the oscillations between the hump and spout states occurring near the transition over periods as short as one minute. Note that the time scale for this effect is still much larger than the time scale for pump-induced noise in the withdrawal rate, which can produce similar effects near the transition. While the increase in the S_u values is most likely due to a uniform reduction in γ over the entire interface, the dynamic nature of the observed hump to spout oscillations implies that the flows may cause local variations in the surfactant concentration. In this picture, when the system is in the hump state, surfactants are dragged toward the hump tip by the surface flows. If the system is sufficiently close to the transition, this accumulation, which lowers the surface tension locally, causes the hump to increase its height and curvature and ultimately drives the system into the spout state. Once in the

spout state, the local surfactant concentration reduces over time and the system eventually decays back into the hump state. This picture is motivated by the observations of de Bruijn [35] for tip streaming of drops under shear flow. While the local boundary conditions for these two problems are different, the flow patterns are remarkably similar indicating that the oscillatory behavior observed in both systems may be correlated.

Since many of the measurements discussed in the paper are performed in the vicinity of the transition, care must be taken when measuring the hump height and curvature. In order to understand how h_{max} and κ change with time, the following experiment is performed. First, the system is placed in the hump state. Then, the flow rate is increased momentarily so that the interface forms a spout for a short period of time. Just after spout collapse, the time dependence of the hump curvature and height is measured. Figures 8(a) and 8(b) show the results of measurements performed for the same system, with the same value of S, but at different values of Q. The initial decay, which occurs over a time scale of about 5 s, gives some measure of the relaxation time for the flows in these systems. Following this initial decay, the height and curvature values plateau. These plateaus are asso-

ciated with a regime where the local surfactant concentration is too low to affect the shape of the interface. When the system is near the transition so that $(Q_c-Q)/Q \approx 0.004$, the plateau regime lasts about 15 s and is followed by a regime in which both the height and curvature increase their values [Fig. 8(a)]. However, as shown by Fig. 8(b), when the experiments are performed at $(Q_c-Q)/Q \approx 0.01$, the plateau regime lasts for over 20 min. When collecting data for the scaling relations, it is important to determine the value of the hump height and mean curvature in the plateau regime. Also, a larger amount of error must be assigned to data points taken from plateau regimes that are short lived. Note, however, that since the plateau regime lengthens quite rapidly as $(Q_c-Q)/Q$ is increased, for the cleaned interface, these precautions only apply to the one or two data points in the scaling relations, which are closest to the transition. For the equilibrated systems, the plateau regimes are shorter and greater caution must be taken in making the measurements. Comparisons between the $(h_c-h_{max})/h_{max}$ versus κ/n curves for equilibrated systems and clean systems indicate that when these precautions are taken there is no change in the scaling curves.

[1] H. E. Edgerton, E. A. Hauser, and W. B. Tucker, J. Appl. Phys. **41**, 1209 (1937).
[2] R. E. Caflisch and G. C. Papanicolaou, in *Singularities in Fluids, Plasmas, and Optics* (Kluwer, Norwell, MA, 1993).
[3] A. L. Bertozzi, M. P. Brenner, T. F. Dupont, and L. P. Kadanoff, *Trends and Perspectives in Applied Mathematics* (Springer, New York, 1994).
[4] R. E. Goldstein, A. I. Pesci, and M. J. Shelley, Phys. Rev. Lett. **70**, 3043 (1993).
[5] M. Pugh and M. J. Shelley, Commun. Pure Appl. Math. **51**, 733 (1998).
[6] J. Eggers, Rev. Mod. Phys. **69**, 865 (1997).
[7] X. D. Shi, M. P. Brenner, and S. R. Nagel, Science **265**, 219 (1994).
[8] D. H. Peregrine, G. Shoker, and A. Symon, J. Fluid Mech. **212**, 25 (1990).
[9] I. Cohen and S. R. Nagel, Phys. Rev. Lett. **88**, 074501 (2002).
[10] G. I. Barenblatt, *Scaling, Self-Similarity and Intermediate Asymptotics* (Cambridge University Press, Cambridge, UK, 1996).
[11] J. R. Lister and H. A. Stone, Phys. Fluids **10**, 2758 (1998).
[12] I. Cohen and S. R. Nagel, Phys. Fluids **13**, 3533 (2001).
[13] I. Cohen, H. Li, J. L. Hougland, M. Mrksich, and S. R. Nagel, Science **292**, 265 (2001).
[14] A. Acrivos and T. S. Lo, J. Fluid Mech. **86**, 641 (1978).
[15] J. T. Jeong and H. K. Moffatt, J. Fluid Mech. **241**, 1 (1992).
[16] J. Eggers, Phys. Rev. Lett. **86**, 4290 (2001).
[17] E. Lorenceau, F. Restagno, and D. Quere, Phys. Rev. Lett. **90**, 184501 (2003).
[18] G. H. Jirka and D. S. Katavola, J. Hydraul. Res. **17**, 53 (1979).
[19] D. F. Harelman, R. L. Morgan, and R. A. Purple, in *Proceedings of the 8th Congress Int. Assoc. Hydraulic Res.* (1959), pp.
10-C-1–10-C-16.
[20] H. Rouse, J. Hydraul. Div., Am. Soc. Civ. Eng. **82**, 1038.3 (1956).
[21] P. Gariel, Houille Blanche **4**, 56 (1949).
[22] A. Craya, Houille Blanche **4**, 44 (1949).
[23] M. Muskat, *Physical Principles of Oil Production* (McGraw-Hill, New York, 1972).
[24] S. Blake and G. N. Ivey, J. Volcanol. Geotherm. Res. **27**, 153 (1986).
[25] J. R. Lister, J. Fluid Mech. **198**, 231 (1989).
[26] J. B. Segur and H. E. Oberstar, Ind. Eng. Chem. **43**, 2117 (1951).
[27] A. W. Neumann and J. K. Spelt, *Applied Surface Thermodynamics* (Marcel-Dekker, New York, 1995).
[28] F. K. Hansen and G. Rodsrud, J. Colloid Interface Sci. **141**, 1 (1991).
[29] D. Quere, Annu. Rev. Fluid Mech. **31**, 347 (1999).
[30] W. W. Zhang (private communication).
[31] A gel permeation chromatography analysis performed by Jordi Associates Inc. on the PDMS used in the experiments shows that while the average molecular weight (M_w) of the PDMS is about 31 000, the distribution is broad and 5% by weight of the chains have a molecular weight of 200 000. Furthermore, even higher molecular weight polymers may be present at concentrations lower than 5% by weight and cannot be detected due to the limitations of this technique.
[32] D. F. James and K. Walters, *Techniques of Rheological Measurement* (Elsevier, New York, 1994).
[33] A. M. Ganan-Calvo, Phys. Rev. Lett. **80**, 285 (1998).
[34] J. D. Sherwood, J. Fluid Mech. **144**, 281 (1984).
[35] R. A. de Bruijn, Chem. Eng. Sci. **48**, 277 (1993).
[36] Since the data points for both curves were not aligned, χ^2 was

calculated in the following way: First a local linear fit was used to interpolate the value of curve$_1$ between the data points. Second, the minimum distance between the interpolated curve and the value of the points in curve$_2$, $\delta_{i,2}$ was calculated. The χ^2 value for the entire curve is defined as: $\chi^2 = 1/N\Sigma\, \delta_{i,2}^2/[\sigma_{1x}^2 + \sigma_{1y}^2 + (\sigma_{2x}^2 + \sigma_{2y}^2)/n]$ where N is the number of points compared, σ_{1x} and σ_{1y} are the experimental errors associated with the x and y points in curve$_1$, σ_{2x} and σ_{2y} are the experimental errors associated with the x and y points in curve$_2$, n is equal to the number of points used in making the

linear fit to curve$_1$, and the sum is taken over the index i, which labels the points in curve$_2$.

[37] The definition is made ambiguous since there are a number of velocity gradients characteristic of the flows near the stagnation point at the hump tip.

[38] It is well known that inertial stresses, which dominate when very low viscosity fluids are used to conduct the selective withdrawal experiments, cannot produce humps of significant height or curvature.